ACS Catalysis

pubs.acs.org/acscatalysis Research Article

Catalytic Reaction Triggered by Magnetic Induction Heating Mechanistically Distinguishes Itself from the Standard Thermal Reaction

Alexander Adogwa,[#] Ewa Chukwu,[#] Alexander Malaj, Venkata R. Punyapu, Owen Chamness, Nicolas Glisson, Bridget Bruce, Sungsik Lee, Michael J. Zachman, David A. Bruce, Rachel B. Getman, O. Thompson Mefford,* and Ming Yang*

Cite This: *ACS Catal.* 2024, 14, 4008–4017 Read Online

ACCESS | Metrics & More | Article Recommendations | Supporting Information

ABSTRACT: As a recent advancement in reaction engineering, magnetic induction heating (MIH) is utilized to initiate the intended reactions by enabling the self-heating of the ferromagnetic catalyst particles. While MIH can be energy-efficient and industrially scalable, its full potential has been underappreciated in catalysis because of the perception that MIH is merely an alternative heating approach. Unexpectedly, we show that the MIH-triggered reaction could go beyond standard thermal catalysis. Specifically, by probing the representative Pt/Fe_3O_4 catalysts with CO oxidation in both thermal and MIH modes with consistent temperature profiles and catalyst structures, we found that the MIH mode boosts the reactivity more than 25 times by modifying Pt−FeO_x interfacial synergies and promoting facile oxidation of the adsorbed carbonyl species by atomic oxygen. As we preliminarily observed, this beneficial MIH catalysis can be translational to other thermal reactions, potentially paving the way to launch MIH catalysis as a distinct reaction category.

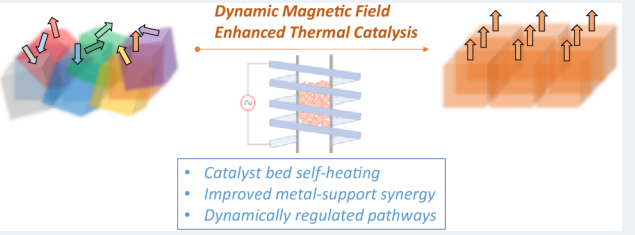

KEYWORDS: *magnetic induction heating, heterogenous catalysis, ferromagnetic catalyst, CO oxidation, reaction kinetics*

1. INTRODUCTION

Magnetic induction heating (MIH) is an alternative heating technique that distinguishes itself from the established combustion and joule heating. Specifically, unlike those apparent heaters, when a magnetic field is applied, it causes magnetic material's unpaired electron spin to align; when the field is reversed, the aligned magnetic moment switches in direction. For many materials exhibiting magnetic anisotropy, magnetic nanoparticles transform magnetic energy from oscillating magnetic fields to heat by hysteresis losses.[1,2] The MIH can be efficient, rapid, and scalable with mild magnetic flux densities,[3−5] and this heating method has made its way into applications, such as metal processing/manufacturing, cooking devices, and tumor treatment.[6−8]

Regarding the ongoing development of MIH in reaction engineering, instead of having the reaction heat supplied toward reaction beds through layers of conduction and convection in conventional setups, a research field that is quickly garnering attention is to develop ferromagnetic catalytic particles (as MIH susceptors) to allow direct and uniform heat generation throughout the catalyst particles in the reaction bed, thereby providing instantaneous reaction light-off and improving energy efficiency.[5,9] As a proof-of-concept, this strategy was recently demonstrated for a variety of thermal catalytic reactions.[4,10−13] Notably, the focal point was to search for and design advanced magnetic nanoparticles for improved heat management by fine-tuning their compositional and structural properties.[14] Speaking of the direct catalysis roles of these ferromagnetic moieties under MIH conditions, they were by default often considered either secondary (not direct catalysis role but just as a heating agent) or identical to their standard thermal catalysis counterparts.

Importantly, at the heart of catalysis, considering that the MIH is a consequence of continuous unpaired electron spin/magnetic moment alignment, which is within the same domain where catalysis can be triggered according to physics, we ask a central question whether the MIH reaction mode, coupled with proper catalysts, shall allow us to mechanistically change the standard thermal catalysis—meaning MIH brings more than just heat and touches the core of how reactions happen.

This remains an unanswered question due to the absence of well-controlled fundamental studies on thermal vs MIH reaction modes. Nevertheless, recent exploratory work from

Received: December 9, 2023
Revised: February 14, 2024
Accepted: February 15, 2024
Published: February 28, 2024

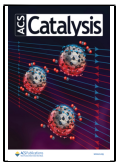

the electrocatalysis community provided an intriguing hint. By exposing the ferromagnetic FeC-Ni catalyst under a high-frequency alternating magnetic field in a cell at about 5 °C, these authors found that the oxygen evolution reaction displayed an enhanced reaction rate that is otherwise only achievable at about 200 °C if following the Arrhenius equation in which the temperature T is the only tuning knob for a given catalyst reaction system.[15] Counterintuitively, this was still a catalytic reaction in a stable aqueous phase without boiling even locally. The projected 200 °C equivalency was never physically captured, and the Tafel slope analyses could not probe to the region that may explicitly suggest kinetic differences. These unexplained results and the associated uncharted research topic propel us to analyze whether and how the catalysis triggered by MIH would intrinsically differ from their standard thermal catalysis, especially when those apparent yet secondary impacts from catalyst structural changes and reaction temperature gradients are carefully excluded.

Herein, we choose the Pt/Fe_3O_4 catalyst as one of the most representative ferromagnetic catalysts for the classic CO oxidation probe reaction, the latter of which involves critical elementary reaction steps, such as dissociative O_2 adsorption, CO adsorption, and *CO and *O transfer that are of broad relevance in fundamental catalysis and industrial applications.[16] The CO oxidation reactivity was evaluated under standard thermal (heat supplied by a tube furnace) and MIH conditions using an identical plug-flow reactor (Figure 1). Notably, our

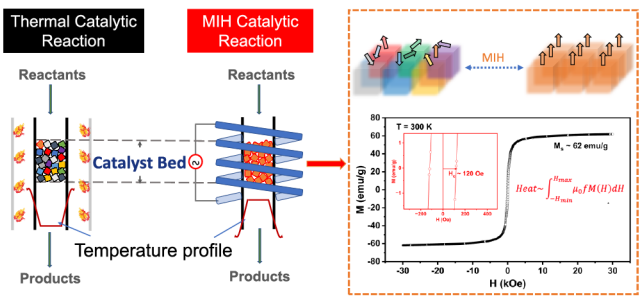

Figure 1. Reactor schematics of standard thermal vs MIH reactions. In the MIH mode, heating occurs through the periodic alignment of the catalyst's magnetic moment in response to the applied dynamic magnetic field (inset, top). The typical magnetic properties of the Pt/Fe_3O_4 catalyst under an oscillating magnetic field (inset, bottom).

results demonstrate that the CO oxidation reaction empowered by MIH must be viewed as a new reaction category from its standard thermal counterpart, where the kinetics are dramatically different. With almost identical reaction temperature and catalyst structures, the reaction catalyzed in the MIH mode proceeded more than one magnitude faster. The shift of reaction pathways and more efficient *CO + *O conversions during the MIH mode are the key contributors. Preliminary encouraging reactivities were observed for preferential oxidation of CO in H_2-rich stream (PROX) and the reverse water−gas shift (RWGS) reactions when studying MIH vs standard thermal reactions with the ferromagnetic catalysts.

2. EXPERIMENTAL DETAILS

2.1. Catalyst Synthesis. To prepare Fe_3O_4 NPs, 25.3 g $Fe(NO_3)_3{\cdot}9H_2O$ was dissolved in 100 mL distilled H_2O, followed by 1 mol/L solution of Na_2CO_3 to precipitate $Fe(OH)_3$ at pH 8. The filtered-out $Fe(OH)_3$ is rinsed multiple times with DI H_2O, and dried at 60 °C for 5 h. The dried $Fe(OH)_3$ was calcined in air at 400 °C for 5 h to obtain Fe_2O_3. Fe_3O_4 is obtained by reducing Fe_2O_3 in 10% H_2/Ar at 400 °C for 45 min with water vapor bubbled through, at a total flow rate of 48 mL/min. Pt is incorporated into the as-prepared Fe_3O_4 NPs by wet impregnation. Specifically, 20 mg of tetraamine platinate (II) nitrate was dissolved in 5 mL H_2O, 250 μL of this solution was then added to 0.5 g Fe_3O_4 NPs to obtain 0.1 wt % Pt/Fe_3O_4. The resulting sample is vacuum-dried overnight at 80 °C, calcined in 96 mL/min argon at 400 °C (ramping rate of 5 °C/min) for 3 h followed by reduction at 200 °C (ramping rate of 5 °C/min) under 10% H_2/Ar with water vapor bubbled at a total flow rate of 48 mL/min for 20 min. Pt/Al_2O_3 was synthesized via wet impregnation.

2.2. Catalysts' Structural and Magnetic Characterizations. X-ray diffraction (XRD) patterns were collected using an X-ray diffractometer (Rigaku D/max 2500) equipped with Cu Kα radiation at a scan rate of 1° min^{-1} in the 2θ range of 20−80°. Transmission electron microscopy (TEM) images for the Fe_3O_4 NPs were acquired at Clemson University's Advanced Materials Research Lab using the Hitachi HT7800 instrument at an accelerating voltage of 100 kV.

Magnetic property measurements were performed on a vibrating sample magnetometer (VSM, Quantum Device PPMS Evercool II). VSM studies were carried out on 13 mg of compact Pt/Fe_3O_4 powder samples that were encapsulated in plastic wrap, fitted into a standard plastic drinking straw, and loaded in a Quantum Design PPMS Dynacool system and sealed under Argon environment. Magnetic measurements were conducted using the ACMS II option at 300 K.

High-angle annular dark-field scanning transmission electron microscopy (HAADF-STEM) of Pt species in the postreaction samples was performed on a Nion UltraSTEM 100 in the Center for Nanophase Materials Sciences (CNMS) at Oak Ridge National Laboratory (ORNL). The instrument was operated at 100 keV with a semiconvergence angle of ∼31 mrad.

X-ray absorption spectroscopy (XAS) scans were conducted in fluorescence mode at the 12-BM of the Advanced Photon Source (APS) at Argonne National Laboratory. The X-ray absorption edge energy for Pt L_3 edge and Fe K edge were calibrated to 11 564 and 7112 eV by Pt foil and Fe foil, respectively, for each scan. Five consecutive scans were acquired for each data collection point. The reference spectra of Pt(II), Pt(0), Fe(III), Fe(0) (i.e., $[Pt(NH_3)_4](NO_3)_2$ − Pt foil and $Fe(NO_3)_3{\cdot}9H_2O$ − Fe foil) were collected. The XANES and EXAFS data were analyzed by the Athena and Artemis software, respectively. The Feff models of Pt foil, PtFe film, and PtO film were used to fit the first shell Pt−Pt, Pt−Fe, and Pt−O coordination numbers, respectively.

Diffuse reflectance infrared Fourier transmission spectroscopy (CO-DRIFTS) experiments were conducted using a Nicolet iS50 FTIR instrument equipped with a liquid nitrogen-cooled MCT detector. Postreaction samples (e.g., after-thermal, after-MIH) weighing 100 mg were loaded into a Harrick Praying Mantis chamber located in the FTIR sample compartment. Samples were purged with 50 sccm of argon (Ar) at room temperature for 30 min and background spectrum collected data by averaging 32 consecutive scans at a resolution of 4 cm^{-1} using the OMNIC Basic Macro programs. Subsequently, CO gas (20 sccm of 5% CO/Ar) was introduced for 45 min before collecting spectra. Each spectrum was an average of 16 consecutive scans. Spectra were processed

https://doi.org/10.1021/acscatal.3c05989
ACS Catal. 2024, 14, 4008−4017

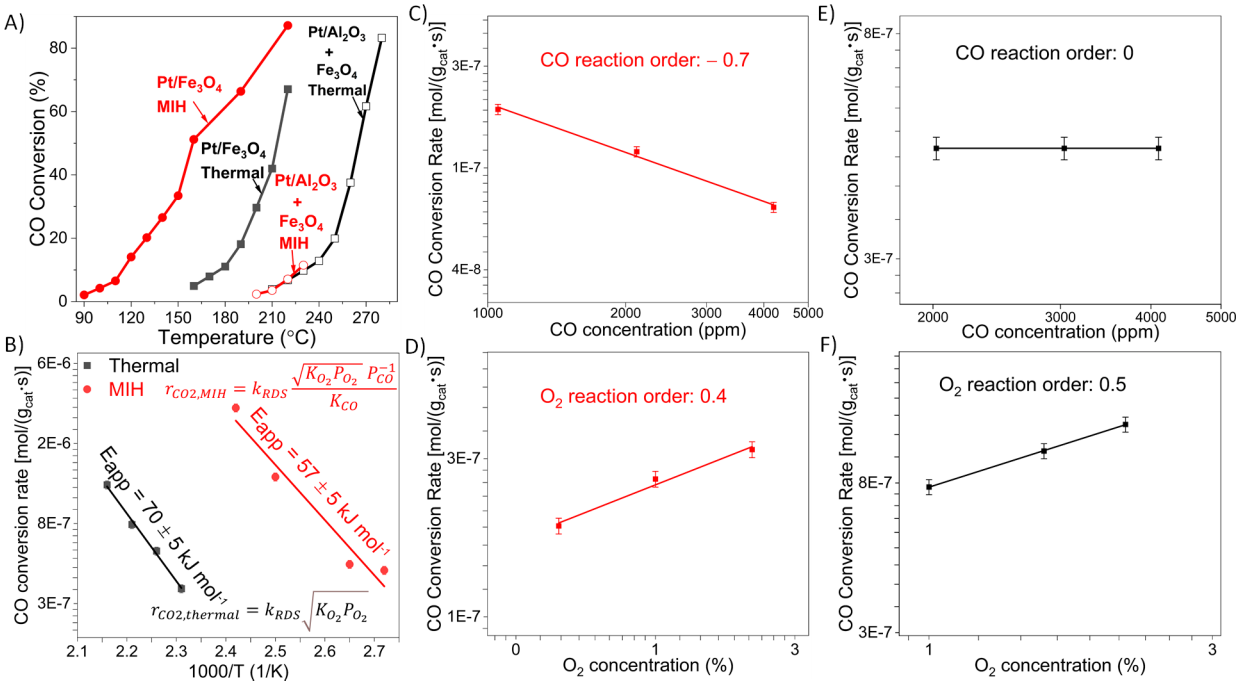

Figure 2. Superior CO oxidation reactivity under MIH compared to standard thermal heating mode. (A) CO oxidation light-off performances for Pt/Fe_3O_4, Pt/Al_2O_3 + Fe_3O_4 in both standard thermal and MIH modes. (B) Arrhenius plots and the most plausible global kinetic expressions for CO oxidation under standard thermal and MIH reaction modes. CO oxidation reaction orders for Pt/Fe_3O_4. (C) CO and (D) O_2 reaction orders in the MIH mode. (E) CO and (F) O_2 reaction orders in the standard thermal heating mode. The reaction orders were determined under kinetic-controlled regimes at 150 °C for MIH ($\mu_0 H$ = 22 mT) and thermal reaction systems, respectively, by fitting to the empirical power rate law for best data repeatability and experimental condition (catalyst amount, flow rate, and feed stream compositions) maneuverability.

using the OMNIC software. Additionally, CO-DRIFTS experiments were performed on KBr under the same conditions to obtain a reference for the removal of the CO gas phase from the spectra of the catalyst samples according to our previous work.[17]

In situ CO + O_2 DRIFTS under MIH was conducted using similar CO-DRIFTS set up above and mimicking our typical reaction condition (20 sccm of 5% CO/Ar, 10 sccm of 10% O_2/Ar). After reaction gas flow for 45 min and collection of spectra, magnetic field (24 mT) was introduced for 25 s, followed by the acquisition of sample spectra. Each spectrum was an average of 8 consecutive scans and processed using the OMNIC software. The gaps in quantifiable CO conversion rates in our in situ CO + O_2 DRIFTS experiment and the light-off data presented in Figure 2A are attributed to the specific conditions employed during this DRIFTS experiment. While 100 mg of catalyst and 30 sccm of reactant gas flow were employed for the in situ CO + O_2 DRIFTS, 100 sccm and 50 mg of catalyst were used in the actual reaction, let alone the DRIFTS cell having a much larger dead volume.

2.3. CO Oxidation Reaction Studies. CO oxidation light-off tests were conducted using a fixed bed tubular quartz reactor at near ambient pressure, with 50 mg of catalyst diluted with 500 mg of quartz sand and supported with quartz wool in the reactor. 100 mL/min of reactant gases composed of 0.5% CO, 0.5% O_2, and balance Ar was utilized for the reaction performed between 160 and 270 °C. Reaction products were monitored with an MKS Series 2000 MultiGas Analyzer and steady-state reaction data were collected.

Similar fixed bed reactor, catalyst loading, and gas flow conditions as in the standard thermal reaction were utilized, and the temperature of the catalyst bed was monitored with Neoptix optic fiber temperature probe and a complementary IR camera. With $\mu_0 H$ = 21−27 mT, reactions were performed between 90 and 220 °C. Reaction products were monitored with an MKS Series 2000 MultiGas Analyzer and steady-state reaction data were collected. Our kinetic data in both reaction modes were obtained by varying catalyst mass between 25 and 60 mg at a flow rate of 100 mL/min, a regime where the CO conversion rates were independent of GHSV. In all cases, the CO conversion was consistently maintained at below 20% to keep the reaction under kinetic control.

The oxygen isotopic exchange experiments were performed at 200 °C with 50 mg of catalyst in the standard thermal and MIH reaction modes ($\mu_0 H$ = 24 mT). In each mode, and at the set temperature, 9 vol % $^{16}O_2$, 9 vol % $^{18}O_2$, balance Ar at a total flow rate of 55 mL/min was introduced. The product distribution was monitored with our online CV-Mass spectrometer using m/z of 32, 34, and 36 respectively.

3. RESULTS AND DISCUSSION

3.1. Enhanced Catalytic Performance of Pt/Fe_3O_4 in the MIH Mode. Our magnetic induction heating system was calibrated with a field−current relationship with a linear fit at ambient conditions (Figure S1). The Pt/Fe_3O_4 nanoparticle catalyst was prepared by impregnating platinum on ferromagnetic Fe_3O_4 presynthesized through water-vapor-assisted hydrogen reduction.[18] Subsequently, the after-impregnation Pt/Fe_3O_4 was dried, calcined, and then reduced mildly by water-assisted hydrogen reduction to obtain the Pt/Fe_3O_4 catalyst to avoid losing ferromagnetism in the case of Fe_2O_3 formations. The catalyst's magnetic properties (saturation magnetization and coercivity) were assessed by vibrating sample magnetometry (VSM) measurements at 300 K. The

https://doi.org/10.1021/acscatal.3c05989
ACS Catal. 2024, 14, 4008−4017

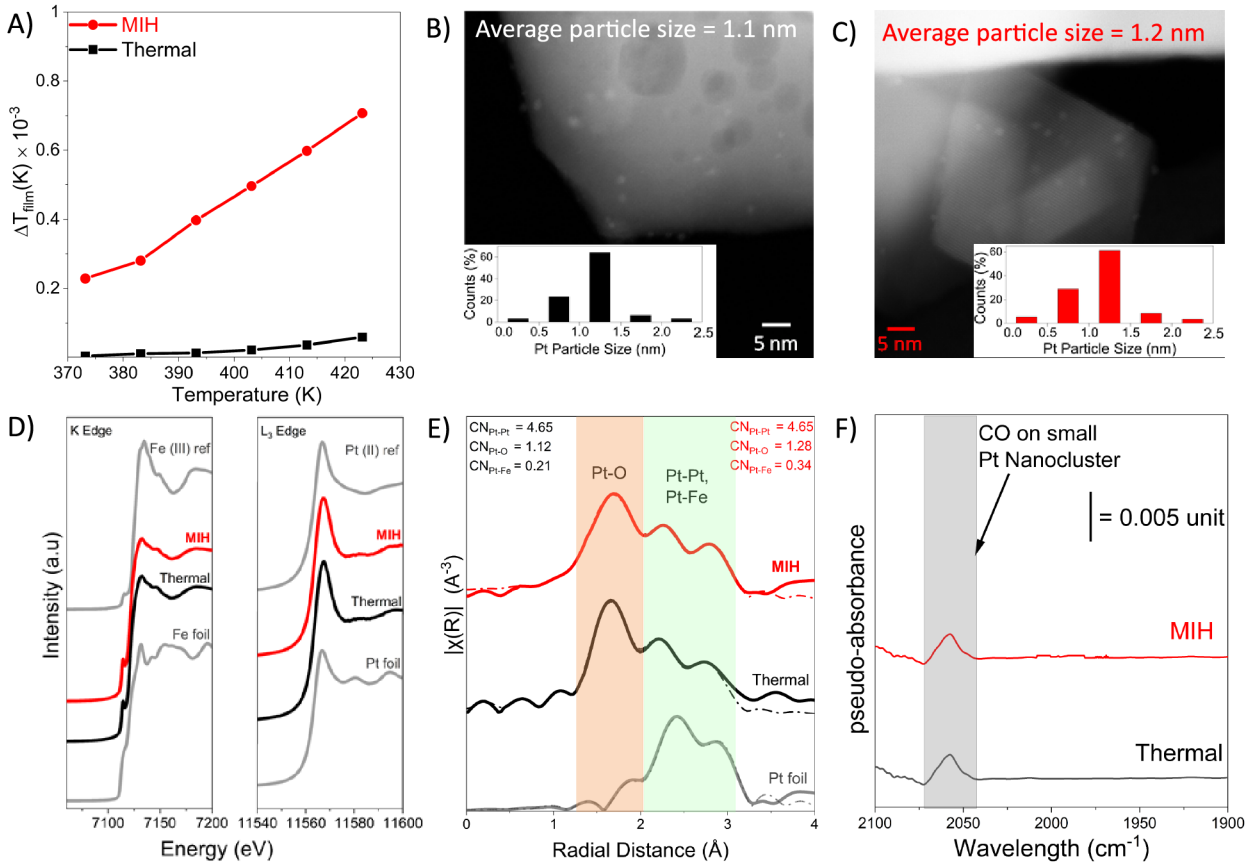

Figure 3. Promoted MIH catalysis in this work is not the consequence of possible reaction temperature differences or changes in catalyst structure−reactivity relationships. (A) Estimated gas-film temperature gradient for catalyst particles in the two reaction modes as a function of the nominal catalyst bed temperatures. (B, C) High-angle annular dark-field scanning transmission electron microscopy (HAADF-STEM) images of reaction-spent Pt/Fe_3O_4 catalysts after thermal and MIH reactions, respectively, and Pt particle size distributions associated with these samples acquired across multiple locations (number of particles measured is ca. 500). (D) Normalized Pt L_3 edge and Fe K edge X-ray absorption near-edge structure (XANES) spectra of reaction-spent Pt/Fe_3O_4 after standard thermal and MIH reactions, (E) Fourier transform of extended X-ray absorption fine structure (EXAFS) spectra of reaction-spent Pt/Fe_3O_4 catalysts after thermal and MIH reactions, (F) diffuse reflectance infrared Fourier transform spectroscopy (DRIFTS) under CO for reaction-spent Pt/Fe_3O_4 at room temperature after subtracting the CO gas phase.

hysteresis loop (Figure 1, *M*−*H* plot inset) suggests an apparent ferromagnetic behavior of the Pt/Fe_3O_4 catalyst. Our analyses of the *M*−*H* curve (Figure 1, *M*−*H* plot inset) show a saturation magnetization (M_s) of 62 emu·g^{-1} and coercivity (H_c) of 9.5 mT, consistent with previously reported values for typical Pt/Fe_3O_4.[19,20] The X-ray diffraction (XRD) patterns of the Pt/Fe_3O_4 catalyst (Figure S2) show an estimated crystallite size of around 23 nm for the Fe_3O_4. Transmission electron microscopy (TEM) images (Figure S3) show a size distribution with ∼70% count frequency of the Fe_3O_4 nanoparticles in the 80 to 120 nm range. Such a size difference indicates the presence of grain boundary walls inside the nominal Fe_3O_4 nanoparticles, which is a possible contributor toward the feasibility of magnetic moment alignment.[21]

The CO oxidation activity of the catalysts in standard thermal and MIH modes, were evaluated under identical conditions. To begin with, the CO oxidation reaction was carried out over a physical mixture of Fe_3O_4 and Pt/Al_2O_3 powders in both reaction modes. As shown in Figure 2A, a physical mixture of Pt/Al_2O_3 particles as the primary catalyst and Fe_3O_4 particles as the heating agent in MIH would display an almost identical reaction light-off curve under both reaction modes, meaning the physically mixed ferromagnetic Fe_3O_4 was mainly used for catalyst bed heating in MIH for the given temperature window, echoing the original perception of MIH reaction as another thermal reaction per se.[22] Next, when Pt/Fe_3O_4 was used as the direct thermal catalyst, the catalyst displayed improved activity from the Pt/Al_2O_3, which is as expected because the Pt−FeO_x interface has been long known to promote the sluggish dissociative O_2 adsorption by using reducible FeO_x supports and to weaken the CO binding on Pt to avoid catalytic site blocking.[23,24] Here, the fascinating finding is that the same catalyst further delivered a magnitude higher activity during the MIH mode if measured against its thermal mode.

3.2. Is the Jump in Reactivity Caused by the Temperature Gaps and the Structure−Reactivity Relationships? To attribute the above reactivity and apparent activation energy (Figure 2A,B) differences to any new catalytic chemistry triggered by MIH, we must exclude (1) errors in temperature measurements due to the different reaction modes and (2) permanent changes in catalyst properties.

For the first caveat, the disparity in intrinsic catalytic performance in the two reactor modes does not stem from inaccurate temperature measurements. This is indirectly indicated by the clearly differed reaction orders for CO and O_2 that we measured in the two reaction modes (Figure 2C−

https://doi.org/10.1021/acscatal.3c05989
ACS Catal. 2024, 14, 4008−4017

F), which should be independent of specific reaction temperatures unless the temperature windows are dramatically different. In a more direct effort, we first confirmed the consistent temperature readings from the fiber optic temperature probe (up to 250 °C) with an IR camera, which reads the reactor wall temperature (showing 2−3 °C temperature lag) in the MIH mode. Similarly, we confirmed negligible differences in temperature measurements by the optic fiber probe and the conventional metal-based thermocouple in the thermal reaction mode, the latter of which cannot be used under MIH conditions due to self-heating. Further, MIH, by its heating mechanism, will indeed bring temperature gradients (ΔT_{film}) between the catalyst particle as the origin and its surrounding bulk medium,[25−28] but the question is whether the ΔT_{film} in our typical plug flow reactor setup is significant enough to distort steady-state catalytic kinetics. The significance of the ΔT_{film} would depend on the magnetic field parameters, reaction conditions, and the capacity of the fluids around the catalyst particles to transport the dissipated heat.[29,30] For example, whereas a temperature difference up to 64 °C was reported for a temperature measurement program executed on Fe_3O_4 in the absence of carrier fluid,[31] other researchers found negligible temperature difference (≤5 °C) as a consequence of the experimental conditions they adopted.[15,26] Our reaction−diffusion−heat transfer analyses for our specific reaction conditions are described in detail (see Notes S1 in Supporting Information), where the MIH-generated heat, reaction heat, heat absorbance by the quartz sand and reaction stream, heat loss to the environment, mass transfer in the surface film, and simultaneous reaction and diffusion inside the catalyst pores were all factored in. As the results summarized in Figure 3A, a negligible surface-to-film temperature gradient in the range of 10^{-3} K for the MIH could not have rendered such significant differences in catalytic reactivity between the two heating modes. We attribute the minimal ΔT_{film} in our MIH reaction system, similar to the situation in the thermal reaction, to the comparatively negligible resistance to heat transfer through the catalyst to the feed stream.[30,32] Hence, the direct kinetic comparisons between the standard thermal and MIH reaction modes are feasible.

For the second caveat, structural changes of the Pt/FeO_x catalysts, if any, can indeed bring significant differences in CO oxidation reactivity.[23,33,34] However, we found that the contribution from this possibility is very limited in our system. This is qualitatively suggested by the same reactivity difference between the MIH and thermal modes after swapping the reaction-spent catalysts (Figure S4). To further confirm this, we characterized our reaction-spent catalysts from the two reaction modes. The XRD patterns of the reaction-spent catalysts from the two reaction modes are almost identical (Figure S2), suggesting that the overall Fe_3O_4 structure of the catalyst is largely intact. Regarding Pt, the dispersion is highly similar for the reaction-spent samples, with average Pt nanocluster (NCs) sizes of ∼1.1 nm and ∼1.2 nm for the thermal and MIH modes, respectively (HAADF-STEM, Figures 3B,C and S5). This similarity continues to show in the XANES (Figure 3D) and the X-ray photoelectron spectroscopy (XPS, Figure S6) results, where the Pt is slightly oxidized, and the Fe is between Fe(II) and Fe(III). The EXAFS of Pt L_3-edge (Figure 3E) for the reaction-spent samples from both reaction modes are also similar, featuring the first-shell coordination for Pt−O (1.1−1.3), Pt−Fe (0.2−0.3), and Pt−Pt (4.7) (Table S1), suggesting an almost identical structure of small Pt clusters anchoring on the FeO_x surfaces through oxygen linkages.[35] This similarity in the local Pt−FeO_x structure is further confirmed by the CO−Pt adsorption peaks with almost identical wavenumbers and intensity in CO-DRIFTS (Figure 3F).[36] Although we acknowledge that it is still possible for certain highly nuanced structural features to escape state-of-the-art characterizations, altogether, we trust that dramatic reactivity difference between the standard thermal and MIH reaction modes cannot be a consequence of any major catalyst structural changes.

3.3. Magnetic Induction Heating Changes CO Oxidation Reaction Pathway. After excluding the possible distortions caused by inaccurate temperature controls and appreciable permanent material property changes, we steered our attention to check how the reaction pathways can be modified to promote catalytic reactivity.

First, the apparent activation energy E_a for the standard thermal mode is noticeably higher than that for the MIH mode (Figure 2B). Further, our measured reaction rate orders with respect to CO and O_2, respectively (Figure 2C−F), show that the kinetics during the two heating modes are different. For the same catalyst, even any imagined differences in the total number of available catalytic sites would not change the apparent activation energy and reaction rate orders.[37,38] Hence, these obvious dissimilarities in apparent activation energies and reaction rate orders suggest that CO oxidation under the two heating modes may have followed quite different reaction pathways.

To interrogate this, we conducted kinetic analyses of possible elementary reaction steps via both Langmuir−Hinshelwood (L−H) and Eley−Rideal (E−R) mechanisms by considering different elementary reaction steps as possible rate-determining steps (RDSs) (see Note S2 in Supporting Information). Scheme 1A − Possibility 3 and Scheme 1B − Possibility 3 in Note S2 were found to fit our experimentally measured data best, where the RDS involves rearrangement of adsorbed carbonyl and oxygen species to produce CO_2. Further, although the reactions in both reaction modes followed the L−H mechanisms, their specific pathways are different. The standard thermal mode follows a dual-site mechanism strictly, where the dual sites refer to Pt surfaces for CO adsorption and the adjacent FeO_x sites for dissociative O_2 adsorption.[24,39] In contrast, the MIH mode follows a quasi-single-site mechanism, which indicates a higher level of synergy between the Pt NCs and Fe_3O_4 substrate to empower the Pt−FeO_x interface as the dominant catalytic center for both reactants, similar to the unique kinetic behavior of the single-atom Pt_1−FeO_x catalysts that maximize the metal−support interfaces as a unified single catalytic site.[16,23] Given the common case of much stronger adsorption of −CO than −O to the transition metal catalytic centers,[40,41] we arrived at simplified kinetic expressions for standard thermal and MIH-triggered catalytic reactions as eqs 1 and 2, respectively, both agreeing reasonably well with the experimentally measured reaction orders:

$$r_{CO_2,thermal} = k_{RDS}\sqrt{K_{O_2}P_{O_2}} \quad (1)$$

$$r_{CO_2,MIH} = k_{RDS}\frac{\sqrt{K_{O_2}P_{O_2}}P_{CO}^{-1}}{K_{CO}} \quad (2)$$

where K_{CO} is the equilibrium constant for the CO adsorption, K_{O_2} is the equilibrium constant for the dissociative

https://doi.org/10.1021/acscatal.3c05989
ACS Catal. 2024, 14, 4008−4017

O_2 adsorption, and k_{RDS} is the rate constant for the RDS involving adsorbed carbonyl and oxygen species.

Their corresponding expressions for the apparent activation energies are

$$E_{app,thermal} = E_{a,RDS} + {}^1/_2 \Delta H_{O_2} \quad (3)$$

$$E_{app,MIH} = E_{a,RDS} + {}^1/_2 \Delta H_{O_2} - \Delta H_{CO} \quad (4)$$

where ΔH_{CO} and ΔH_{O_2} are the reaction enthalpies (negative to heats of adsorption) with $E_{a,RDS}$ being the corresponding activation energy for the RDS step in both reaction modes.

We note that the specific values of the above-derived parameters could be different for the thermal and MIH modes. Considering $K_{CO}P_{CO}$ is much larger than 1 to reflect the favorable CO adsorption (also indicated by the zero to negative CO reaction orders) and ΔH_{CO} being negative, the observed promotional effect by MIH can be the consequences of (1) enhanced dissociative O_2 adsorption (larger K_{O_2} and more negative ΔH_{O_2} for the MIH mode) and/or (2) accelerated RDS (larger k_{RDS} at low temperatures and smaller $E_{a,RDS}$ for the MIH mode).

To probe our hypothesis about the enhanced dissociative O_2 adsorption, we conducted $^{16}O_2/^{18}O_2$ isotope exchange experiments. The chosen reaction temperatures where appreciable CO oxidation reaction happened in both systems and the $^{16}O_2/^{18}O_2$ isotope exchange at these temperatures would disclose the differences, if any, in O_2 adsorption/activation. However, we observed limited differences in the level of oxygen exchange, with the exchange adequately at equilibrium and similar for both systems, as reflected by the almost identical steady-state concentrations of $^{16}O_2$, $^{18}O_2$, and the product, $O^{16}O^{18}$ (Figure 4A for 200 °C and Figure S7 for 100 °C). These phenomena suggest that the kinetically equilibrated dissociative O_2 adsorption step could not have been responsible for the dramatically promoted CO oxidation catalysis in MIH relative to the standard thermal catalysis. We reason that the equilibrium constant K_{O2} for the dissociative O_2 adsorption step remains largely the same in the two reaction modes, meaning any extra reaction Gibbs energy ΔG_{MIH} caused by the MIH at a given temperature is practically very small. This assessment aligns with the earlier work of Steiner and Ulrich,[42] where the contribution of magnetic field effects on altering the chemical reaction equilibrium at even imagined strong magnetic field strengths (B_0, equivalent to 1 T vs up to 27 mT in our case) and magnetic molar susceptibility ($\Delta\chi_M$, 0.01 cm^3/mol) is negligible.

With the enhancement of dissociative O_2 adsorption toward the faster overall kinetics excluded, we narrowed down the possible contributor to the nominally common RDS in both reaction modes, where the adsorbed carbonyl and oxygen species react to produce CO_2. To exclude possible effects of MIH in CO adsorption on the catalyst prior to the RDS, we conducted DRIFTS under CO-only gas flow at 25 °C to determine if there would be any discernible change in CO adsorption induced by the magnetic field following previous procedures. After introducing the magnetic field, the *CO−Pt centered at 2063 cm^{-1} retained almost identical peak intensity and wavenumbers with the spectra before the introduction of the magnetic field (Figure S8). We employed in situ CO + O_2 DRIFTS (Figure 4B) to interrogate whether the MIH mode

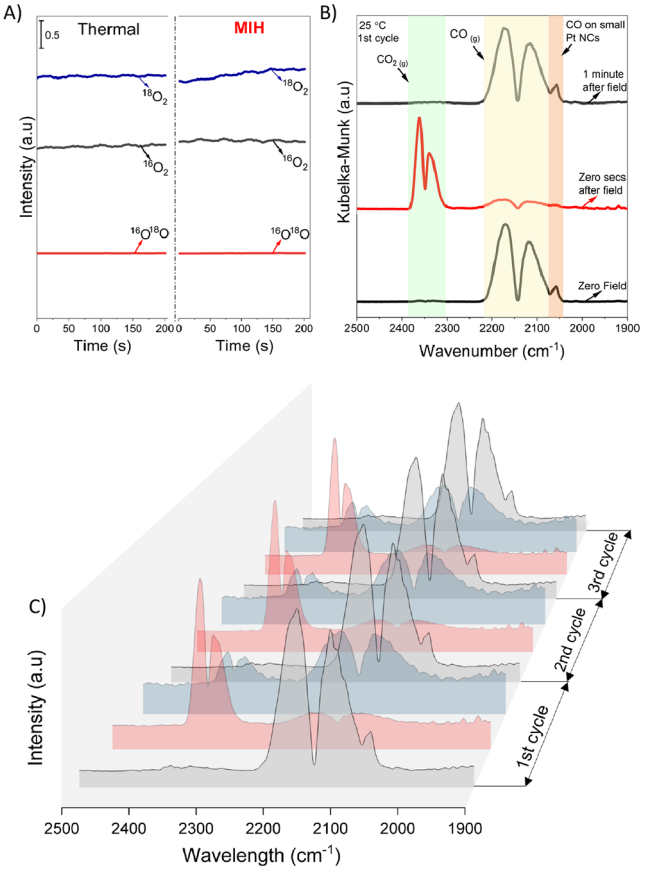

Figure 4. Dynamic magnetic field facilitates CO oxidation under the MIH mode. (A) O_2 isotopes exchange experiments at 200 °C, both the standard thermal and MIH heating modes exhibit comparable O_2 dissociation capabilities. (B) In situ DRIFTS under CO oxidation reaction at 25 °C unlike the thermal-only condition (black), *CO−Pt peak disappears, followed by enhanced CO_2 formation at room temperature after introducing the magnetic field (red spectra). The *CO−Pt peak reappears after the MIH is put off, and the magnetic field effect vanishes. (C) Repeatable cycles of (B) showing the enhanced CO_2 formation with introducing the MIH at room temperature. Starting with the thermal-only condition (gray-filled spectra), the dominant *CO−Pt peak is present but vanishes with introducing the MIH, accompanied by transient CO_2 formation (red-filled spectra). The cycle is completed by gradually returning to the initial thermal-only condition (blue-filled spectra) when the MIH is off, and the magnetic field effect vanishes with time. We note the significant contribution of the environmental CO_2 to the resultant CO_2 formation (ca. 75% contribution)—a consequence of briefly opening the sample chamber for 25 s. As a result, the depicted CO_2 formed should be interpreted qualitatively rather than quantitatively.

indeed benefitted the RDS by allowing facile conversion of the adsorbed carbonyl species. At 25 °C, we observed the dominant atop *CO−Pt centered at 2063 cm^{-1}, the gaseous CO (2118 and 2171 cm^{-1}), and a negligible amount of gaseous CO_2 (2400−2300 cm^{-1}). Upon introducing the oscillating magnetic field of 24 mT for a brief duration of 25 s (to avoid significant temperature fluctuation), the IR spectra collected immediately afterward indicate the prominent formation of gaseous CO_2, accompanied by an almost complete depletion of *CO−Pt and significant consumption of gaseous CO, all indicating the onset of facile *CO oxidation. Upon removing the magnetic field for about 60 s, the DRIFTS spectra of the sample returned to the identical pattern for the initial thermal-

https://doi.org/10.1021/acscatal.3c05989
ACS Catal. 2024, 14, 4008−4017

only condition. This cyclic behavior was consistently observed over multiple cycles (Figure 4C), indicating that the MIH promotional effect is transient. Remarkably, only about 3−4 °C temperature fluctuation was observed for each cycle during the transient MIH mode. Such a minor temperature increase could not have yielded a dramatic change in conversion rate based on the measured apparent activation energy for the standard thermal reaction mode (Figure 2B). Other control experiments by mimicking a sole thermal runaway to 60 °C for Pt/Fe_3O_4 (Figure S9) and a sole heating function of Fe_3O_4 for Pt/Al_2O_3 (Figure S10) failed to deliver the exciting activity associated with the promoted RDS, as expected. The MIH-enabled facile conversion of carbonyl species also suggests that the activation energy $E_{a,RDS}$ (associated with k_{RDS}) in the MIH mode must be significantly lower than the $E_{a,RDS}$ in the standard thermal mode, thereby justifying the lower apparent activation energy for MIH in comparison to the thermal mode (Figure 2B).

The possible modulation of intrinsic catalytic reaction chemistry by oscillating magnetic field as seen for CO oxidation might be translational to diverse thermal catalytic reactions. For example, we equally found similar MIH-promoted reactivities in our preliminary investigations of preferential CO oxidation reaction (PROX) and reverse water−gas shift (RWGS) reaction, compared to the standard thermal reaction. For the PROX (Figure S11A,B), in sharp contrast to the lower activity and negligible CO_2 selectivity in standard thermal mode (Figure S11A), the MIH mode renders enhanced low-temperature activity and over 50% CO_2 selectivity (Figure S11B). Similar striking differences in reactivity are observed for the RWGS (Figure S11C), where the comparative high-temperature activity in the standard thermal reaction mode significantly lags the low-temperature activity and near-equilibrium CO_2 conversions achievable under the MIH mode. Notably, the hydrogen isotope exchange experiment confirms that the superior catalytic performance of Pt/Fe_3O_4 in RWGS during the MIH mode cannot be attributable to the slightly differed hydrogen activation capabilities (Figure S12). This again suggests that the promotional role of MIH for any elementary reaction steps should be generalized with caution. The impact of MIH on transient RDS can be much more significant than on those quasi-equilibrated steps, which was suggested earlier by theory[42] and now proven by our case studies on CO oxidation by Pt/Fe_3O_4 catalysts.

3.4. Possibilities for Critical Considerations. At this stage, we caution our readers that it would be too early to conclude that certain catalyst properties or magnetic field parameters are the definite descriptors to fully explain and predict the MIH promotion effects over the standard thermal reaction. We suggest a few possible critical considerations to explore further. While it is infeasible to decouple and rank these speculations in this report, we hope to highlight these potential MIH descriptors in enriching the tuning strategies for standard thermal reactions.

3.4.1. Catalytic Site Availability. A recent work using a static magnetic field argued that the catalytically desired electron spin conditions had been naturally associated with each catalytic domain already, and the observed enhancement in electrocatalytic reactivity was due to the evolution of multidomain, as featured in heterogeneous catalysts in general, to single-domain states, known as domain wall dynamics, caused by magnetization. According to Ren et al.,[43] the authors deliberately controlled the particle size of their ferromagnetic $CoFe_2O_4$ catalyst to 8 nm, resulting in this ostensibly single-domain material exhibiting nearly equivalent OER reactivity without any external magnetic field to a multidomain $CoFe_2O_4$ with an external magnetic field enhancement. Notably, the multidomain $CoFe_2O_4$ could not deliver the same good OER reactivity without the external magnetic field, so the enhanced OER reactivity of the more common multidomain ferromagnetic catalyst under the external magnetic field could be linked to the possibility of the boundary wall collapse—effectively making the multidomain larger nanoparticle catalytically behaving like a much smaller single-domain catalyst. The alignment of the multidomain catalyst particle in the direction of the external magnetic field could have resulted in the creation of more available active sites to improve the overall reactivity. In our case, we estimate the particle size of Fe_3O_4 to be near 100 nm by TEM imaging (Figure S3), and this exceeds the well-received critical size of Fe_3O_4 single-domain nanoparticles around 26−40 nm.[44] Additionally, the supported Pt NCs have an average size of ∼1 nm, where each Pt atom within those moieties would inherit a different coordination environment and, thus, different interactions with the Fe_3O_4. Therefore, our heterogeneous catalyst, being multidomain in nature, could have potentially undergone periodic boundary wall collapse through the continuous alignment of its domains under the alternating magnetic field. Microscopically, these possible alignment effects may render our catalysts to inherit a more homogenized $Pt−FeO_x$ interface in the similitude of a quasi-single-site that maximizes the CO* and O* interactions for the subsequent CO_2* formation. However, the singular driving force of increasing catalytic site availability could not justify the more dramatic change of reaction energetics revealed by our kinetics and in situ characterizations.

3.4.2. Dynamic Alignment of Unpaired Electrons. Albeit adopting much stronger yet static magnetic fields (e.g., 0.35−1.25 T) for electrocatalytic OER, where the sole focus was on the triplet O_2, recent studies have implicated the significance of spin alignment and spin-selective electron transfer in static magnetic field assisted catalysis.[45−48] Through experimental observations and density functional theory (DFT) calculations, these works suggest that magnetization-induced alignment of magnetic domains and their spins within ferromagnetic catalysts promotes spin polarization and spin-selective electron transfer, leading to enhanced oxygen evolution by the breakage of two water molecules to produce a paramagnetic triplet oxygen molecule through spin conversion. However, we did not notice any appreciable promotion or inhibition for the dissociative O_2 activation step in our reaction setting, possibly due to the elevated temperatures used in the reaction and the slim chance for O_2 dissociation to present as RDS. Nevertheless, we infer that the general concept of how static magnetic fields promote triplet O_2 formations may be translational to the dynamic field for at least a quarter cycle (from zero to max field). For example, extra ligand stabilization energy can be created by the magnetic field by promoting the high-spin states for Fe^{2+} (d^5) and Fe^{3+} (d^6) to facilitate catalyst−adsorbate interactions, and the ferromagnetic polarization effect on iron can be further cascaded to Pt^{2+} (d^8) through the transferred lone electron through the −O− linkage, according to the Goodenough−Kanamori rule. Hence, the Pt−O−Fe interfaces with a higher density of unpaired electrons may be more energetically preferred to bind the weakly electrophilic CO_2 through carbon in the η^1 or η^2 mode, lowering the reaction activation energy for the *CO + *O →

https://doi.org/10.1021/acscatal.3c05989
ACS Catal. 2024, 14, 4008−4017

*CO_2 step according to linear scaling relationship between reaction enthalpy and activation energy.

Indeed, the interaction and chemical reactivities of adsorbates with magnetic catalyst would depend on the catalyst surface spin states.[49] We note that the same effect of the spin states may promote *CO adsorption as well due to the higher extent of π backbonding from Pt to C. We suspect this static magnetic effect may, in fact, lead to undesired catalyst surface poisoning by CO. For example, in sharp contrast to our observed enhanced reactivity for CO oxidation under an oscillating magnetic field, the presence of an external magnetic field was found to compromise CO oxidation over a Pt-supported 'carbon-capped Co magnetic nanocore' catalyst.[50] Through in situ resonant inelastic X-ray scattering (RIXS) studies, the authors reported that the static magnetic field's interaction with the magnetic catalyst support altered the electronic structure of Pt, resulting in a stronger CO adsorption geometry on Pt, frustrating the overall catalysis. Intriguingly, the negative CO reaction order in the dynamic MIH reaction mode in our case, though signaling strong *CO adsorption at least for some duration, does not translate to the inhibition of the overall reactivity. This is highly unusual for conventional steady-state CO oxidation reactions.

This leads to the next critical possibility—the periodic optimization of catalyst surfaces' binding properties. In view of the oscillating magnetic field applied during the MIH reaction, we infer that there is a possibility of dynamic chemistry between the intermediates and the catalyst surface due to the periodic alignment/dealignment of lone electrons at the interface at high frequency. We embrace the possibility that the dynamic magnetic perturbation at 205 kHz in our work improves the RDS by breaking the Sabatier limit. According to a series of model kinetic studies by Ardagh et al.[22] and Gathmann et al.[51] modulating catalyst electronic properties to separately optimize the product formation (in adsorbed state) and product desorption steps at high frequencies (e.g., > 10 Hz for a model A* → B+* thermal reaction) is a promising concept to eclipse the compromise set by the Sabatier volcano plot, where the reaction intermediate should avoid binding to the catalyst surfaces either too weakly or too strongly to achieve high activity. By modifying the binding energies of surface intermediates (e.g., A* and B*) over a broad range of frequencies ($10^{-4} < f < 10^{11}$ s^{-1}), they interrogated the catalytic activity of a simulated catalyst surface oscillating between two distinct electronic states. When the frequency of oscillating surface energy states allows the most abundant B* formation from A* →B* before switching to favor B* → B+*, significant improvements in catalytic turnover frequencies above the Sabatier maximum can be achieved. With the experimental findings from MIH, we infer that the high-frequency oscillating magnetic field may have served as a convenient and scalable control module to guide the Pt−Fe_3O_4 interfaces to reach electronic configurations that energetically favor the formation of *CO_2 (when the field is increasing/on) and CO_2 desorption (when the field is fading/off), dynamically, where the undesired strong binding of *CO is only temporary. To what extent this hypothesis holds requires systematic mechanistic studies involving static field versus dynamic field as well as a broad range of magnetic energy and oscillating frequencies.

4. CONCLUSIONS

Unlike the emerging electro-, photo-, and plasma-catalysis that can leverage overpotentials, freed electrons, or energized radicals, respectively, as the extra tuning knobs to control reactions, standard thermal catalysis relies solely on the temperatures to tune the reactivity for a given catalyst without any dynamic field enhancement. In this work, we demonstrated that MIH-based catalysis provides new possibilities in advancing conventional thermal reactions by not only manipulating apparent reaction temperatures but reaction pathways as well. Given many industrially important catalysts involve ferromagnetic transition metals, such as Fe, Co, Ni, and Mn, our findings may further inspire dedicated catalytic materials' design and reaction control research activities to better harness the MIH impact.

■ ASSOCIATED CONTENT

Supporting Information

The Supporting Information is available free of charge at https://pubs.acs.org/doi/10.1021/acscatal.3c05989.

Field calibration, XRD measurements of as-synthesized and spent catalyst, TEM images of Fe_3O_4, representative HAADF-STEM images, XPS measurements, EXAFS fitting parameters, O_2 isotope measurements, in situ CO-DRIFTS, preliminary reaction data for PROX and RWGS reactions, H_2-D_2 isotope measurements, heat and diffusion analysis, kinetic expression analyses (PDF)

■ AUTHOR INFORMATION

Corresponding Authors

O. Thompson Mefford − *Materials Science and Engineering, Clemson University, Clemson, South Carolina 29634, United States;* orcid.org/0000-0002-9164-2521; Email: mefford@clemson.edu

Ming Yang − *Chemical and Biomolecular Engineering, Clemson University, Clemson, South Carolina 29634, United States;* orcid.org/0000-0002-6321-8854; Email: myang3@clemson.edu

Authors

Alexander Adogwa − *Chemical and Biomolecular Engineering, Clemson University, Clemson, South Carolina 29634, United States*

Ewa Chukwu − *Chemical and Biomolecular Engineering, Clemson University, Clemson, South Carolina 29634, United States*

Alexander Malaj − *Materials Science and Engineering, Clemson University, Clemson, South Carolina 29634, United States*

Venkata R. Punyapu − *Chemical and Biomolecular Engineering, Clemson University, Clemson, South Carolina 29634, United States;* Present Address: Chemical and Biomolecular Engineering, Ohio State University, Columbus, OH 43210-1226

Owen Chamness − *Chemical and Biomolecular Engineering, Clemson University, Clemson, South Carolina 29634, United States*

Nicolas Glisson − *Chemical and Biomolecular Engineering, Clemson University, Clemson, South Carolina 29634, United States*

https://doi.org/10.1021/acscatal.3c05989
ACS Catal. 2024, 14, 4008−4017

Bridget Bruce − *Chemical and Biomolecular Engineering, Clemson University, Clemson, South Carolina 29634, United States*

Sungsik Lee − *X-Ray Science Division, Argonne National Laboratory, Argonne, Illinois 60439, United States;* orcid.org/0000-0002-1425-9852

Michael J. Zachman − *Center for Nanophase Materials Sciences, Oak Ridge National Laboratory, Oak Ridge, Tennessee 37831, United States*

David A. Bruce − *Chemical and Biomolecular Engineering, Clemson University, Clemson, South Carolina 29634, United States*

Rachel B. Getman − *Chemical and Biomolecular Engineering, Clemson University, Clemson, South Carolina 29634, United States;* Present Address: Chemical and Biomolecular Engineering, Ohio State University, Columbus, OH 43210-1226; orcid.org/0000-0003-0755-0534

Complete contact information is available at: https://pubs.acs.org/10.1021/acscatal.3c05989

Author Contributions

#A.A. and E.C. contributed equally to this work.

Notes

The authors declare no competing financial interest.

■ ACKNOWLEDGMENTS

M.Y. thanks the support provided by the start-up fund of Clemson University, the National Science Foundation Award 2146591, and the American Chemical Society PRF Doctoral New Investigator Award 65606-DNI5. The use of 12-BM beamline of the Advanced Photon Source is supported by the U.S Department of Energy (DOE) Office of Science User Facility operated for the DOE Office of Science by the Argonne National Laboratory (Contract No. DE-ACO2-06CH11357). The electron microscopy experiments of this research was supported by the Center for Nanophase Material Sciences (CNMS), which is a U.S. Department of Energy, Office of Science User Facility at Oak Ridge National Laboratory. A.A. would like to use this research article to celebrate my advisor's newborn daughter, Caroline. A.A. acknowledges the contribution of Ella Shi, a high school student at Redmond High School, Redmond, Washington, for her contribution to the reactor figures. M.Y. and O.T.M. would like to acknowledge the artwork by the Clemson University Marketing and Communications Division.

■ REFERENCES

(1) Hergt, R.; Dutz, S.; Müller, R.; Zeisberger, M. Magnetic Particle Hyperthermia: Nanoparticle Magnetism and Materials Development for Cancer Therapy. *J. Phys. Condens. Matter* **2006**, *18* (38), S2919.

(2) Martínez-Prieto, L. M.; Marbaix, J.; Asensio, J. M.; Cerezo-Navarrete, C.; Fazzini, P. F.; Soulantica, K.; Chaudret, B.; Corma, A. Ultrastable Magnetic Nanoparticles Encapsulated in Carbon for Magnetically Induced Catalysis. *ACS Appl. Nano Mater.* **2020**, *3* (7), 7076−7087.

(3) Bordet, A.; Lacroix, L.-M.; Fazzini, P.-F.; Carrey, J.; Soulantica, K.; Chaudret, B. Magnetically Induced Continuous CO_2 Hydrogenation Using Composite Iron Carbide Nanoparticles of Exceptionally High Heating Power. *Angew. Chem.* **2016**, *128* (51), 16126−16130.

(4) Meffre, A.; Mehdaoui, B.; Connord, V.; Carrey, J.; Fazzini, P. F.; Lachaize, S.; Respaud, M.; Chaudret, B. Complex Nano-Objects Displaying Both Magnetic and Catalytic Properties: A Proof of Concept for Magnetically Induced Heterogeneous Catalysis. *Nano Lett.* **2015**, *15* (5), 3241−3248.

(5) Wang, W.; Tuci, G.; Duong-Viet, C.; Liu, Y.; Rossin, A.; Luconi, L.; Nhut, J. M.; Nguyen-Dinh, L.; Pham-Huu, C.; Giambastiani, G. Induction Heating: An Enabling Technology for the Heat Management in Catalytic Processes. *ACS Catal.* **2019**, *9* (9), 7921−7935.

(6) Ha, P. T.; Le, T. T. H.; Bui, T. Q.; Pham, H. N.; Ho, A. S.; Nguyen, L. T. Doxorubicin Release by Magnetic Inductive Heating and in Vivo Hyperthermia-Chemotherapy Combined Cancer Treatment of Multifunctional Magnetic Nanoparticles. *New. J. Chem.* **2019**, *43* (14), 5404−5413.

(7) Revia, R. A.; Zhang, M. Magnetite Nanoparticles for Cancer Diagnosis, Treatment, and Treatment Monitoring: Recent Advances. *Mater. Today* **2016**, *19* (3), 157−168.

(8) N'Guyen, T. T. T.; Duong, H. T. T.; Basuki, J.; Montembault, V.; Pascual, S.; Guibert, C.; Fresnais, J.; Boyer, C.; Whittaker, M. R.; Davis, T. P.; Fontaine, L. Functional Iron Oxide Magnetic Nanoparticles with Hyperthermia-Induced Drug Release Ability by Using a Combination of Orthogonal Click Reactions. *Angew. Chem. Int. Ed.* **2013**, *52* (52), 14152−14156.

(9) Almind, M. R.; Vendelbo, S. B.; Hansen, M. F.; Vinum, M. G.; Frandsen, C.; Mortensen, P. M.; Engbæk, J. S. Improving Performance of Induction-Heated Steam Methane Reforming. *Catal. Today* **2020**, *342*, 13−20.

(10) Ceylan, S.; Friese, C.; Lammel, C.; Mazac, K.; Kirschning, A. Inductive Heating for Organic Synthesis by Using Functionalized Magnetic Nanoparticles inside Microreactors. *Angew. Chem. Int. Ed.* **2008**, *47* (46), 8950−8953.

(11) Vinum, M. G.; Almind, M. R.; Engbæk, J. S.; Vendelbo, S. B.; Hansen, M. F.; Frandsen, C.; Bendix, J.; Mortensen, P. M. Dual-Function Cobalt−Nickel Nanoparticles Tailored for High-Temperature Induction-Heated Steam Methane Reforming. *Angew. Chem. Int. Ed.* **2018**, *57* (33), 10569−10573.

(12) Kale, S. S.; Asensio, J. M.; Estrader, M.; Werner, M.; Bordet, A.; Yi, D.; Marbaix, J.; Fazzini, P. F.; Soulantica, K.; Chaudret, B. Iron Carbide or Iron Carbide/Cobalt Nanoparticles for Magnetically-Induced CO_2 Hydrogenation over Ni/SiRAlO$_x$ Catalysts. *Catal. Sci. Technol.* **2019**, *9* (10), 2601−2607.

(13) Rivas-Murias, B.; Asensio, J. M.; Mille, N.; Rodríguez-González, B.; Fazzini, P. F.; Carrey, J.; Chaudret, B.; Salgueiriño, V. Magnetically Induced CO_2 Methanation Using Exchange-Coupled Spinel Ferrites in Cuboctahedron-Shaped Nanocrystals. *Angew. Chem. Int. Ed.* **2020**, *59* (36), 15537−15542.

(14) Bordet, A.; Lacroix, L. M.; Fazzini, P. F.; Carrey, J.; Soulantica, K.; Chaudret, B. Magnetically Induced Continuous CO_2 Hydrogenation Using Composite Iron Carbide Nanoparticles of Exceptionally High Heating Power. *Angew. Chem. Int. Ed.* **2016**, *55* (51), 15894−15898.

(15) Niether, C.; Faure, S.; Bordet, A.; Deseure, J.; Chatenet, M.; Carrey, J.; Chaudret, B.; Rouet, A. Improved water electrolysis using magnetic heating of FeC−Ni core−shell nanoparticles. *Nat. Energy* **2018**, *3* (6), 476−483.

(16) Wang, H.; Liu, J. X.; Allard, L. F.; Lee, S.; Liu, J.; Li, H.; Wang, J.; Wang, J.; Oh, S. H.; Li, W.; Flytzani-Stephanopoulos, M.; Shen, M.; Goldsmith, B. R.; Yang, M. Surpassing the Single-Atom Catalytic Activity Limit through Paired Pt-O-Pt Ensemble Built from Isolated Pt_1 Atoms. *Nat. Commun.* **2019**, *10* (1), 3808.

(17) Chukwu, E.; Molina, L.; Rapp, C.; Morales, L.; Jin, Z.; Karakalos, S.; Wang, H.; Lee, S.; Zachman, M. J.; Yang, M. Crowded Supported Metal Atoms on Catalytically Active Supports May Compromise Intrinsic Activity: A Case Study of Dual-Site Pt/α-MoC Catalysts. *Appl. Catal., B* **2023**, *329*, 122532.

(18) Zieliński, J.; Zglinicka, I.; Znak, L.; Kaszkur, Z. Reduction of Fe_2O_3 with Hydrogen. *Appl. Catal., A* **2010**, *381* (1−2), 191−196.

(19) Guardia, P.; Labarta, A.; Batlle, X. Tuning the Size, the Shape, and the Magnetic Properties of Iron Oxide Nanoparticles. *J. Phys. Chem. C* **2011**, *115* (2), 390−396.

(20) Li, Q.; Kartikowati, C. W.; Horie, S.; Ogi, T.; Iwaki, T.; Okuyama, K. Correlation between Particle Size/Domain Structure

and Magnetic Properties of Highly Crystalline Fe_3O_4 Nanoparticles. *Sci. Rep.* **2017**, *7* (1), 9894.
(21) Ren, X.; Wu, T.; Gong, Z.; Pan, L.; Meng, J.; Yang, H.; Dagbjartsdottir, F. B.; Fisher, A.; Gao, H. J.; Xu, Z. J. The Origin of Magnetization-Caused Increment in Water Oxidation. *Nat. Commun.* **2023**, *14* (1), 2482.
(22) Ardagh, M. A.; Abdelrahman, O. A.; Dauenhauer, P. J. Principles of Dynamic Heterogeneous Catalysis: Surface Resonance and Turnover Frequency Response. *ACS Catal.* **2019**, *9* (8), 6929−6937.
(23) Qiao, B.; Wang, A.; Yang, X.; Allard, L. F.; Jiang, Z.; Cui, Y.; Liu, J.; Li, J.; Zhang, T. Single-Atom Catalysis of CO Oxidation Using Pt_1/FeO_x. *Nat. Chem.* **2011**, *3* (8), 634−641.
(24) Liu, L.; Zhou, F.; Wang, L.; Qi, X.; Shi, F.; Deng, Y. Low-Temperature CO Oxidation over Supported Pt, Pd Catalysts: Particular Role of FeO_x Support for Oxygen Supply during Reactions. *J. Catal.* **2010**, *274* (1), 1−10.
(25) da Silva Moura, N.; Bajgiran, K. R.; Melvin, A. T.; Dooley, K. M.; Dorman, J. A. Direct Probing of Fe_3O_4 Nanoparticle Surface Temperatures during Magnetic Heating: Implications for Induction Catalysis. *ACS Appl. Nano Mater.* **2021**, *4* (12), 13778−13787.
(26) Faure, S.; Mille, N.; Kale, S. S.; Asensio, J. M.; Marbaix, J.; Farger, P.; Stoian, D.; Van Beek, W.; Fazzini, P. F.; Soulantica, K.; Chaudret, B.; Carrey, J. Internal Temperature Measurements by X-Ray Diffraction on Magnetic Nanoparticles Heated by a High-Frequency Magnetic Field. *J. Phys. Chem. C* **2020**, *124* (40), 22259−22265.
(27) Keblinski, P.; Cahill, D. G.; Bodapati, A.; Sullivan, C. R.; Taton, T. A. Limits of Localized Heating by Electromagnetically Excited Nanoparticles. *J. Appl. Phys.* **2006**, *100* (5), 054305.
(28) Cazares-Cortes, E.; Cabana, S.; Boitard, C.; Nehlig, E.; Griffete, N.; Fresnais, J.; Wilhelm, C.; Abou-Hassan, A.; Ménager, C. Recent Insights in Magnetic Hyperthermia: From the "Hot-Spot" Effect for Local Delivery to Combined Magneto-Photo-Thermia Using Magneto-Plasmonic Hybrids. *Adv. Drug Delivery Rev.* **2019**, *138*, 233−246.
(29) Mortensen, P. M.; Engbæk, J. S.; Vendelbo, S. B.; Hansen, M. F.; Østberg, M. Direct Hysteresis Heating of Catalytically Active Ni−Co Nanoparticles as Steam Reforming Catalyst. *Ind. Eng. Chem. Res.* **2017**, *56* (47), 14006−14013.
(30) Varsano, F.; Bellusci, M.; La Barbera, A.; Petrecca, M.; Albino, M.; Sangregorio, C. Dry Reforming of Methane Powered by Magnetic Induction. *Int. J. Hydrogen. Energy* **2019**, *44* (38), 21037−21044.
(31) da Silva Moura, N.; Bajgiran, K. R.; Melvin, A. T.; Dooley, K.; Dorman, J. Direct Probing of Fe_3O_4 Nanoparticle Surface Temperatures during Magnetic Heating: Implications for Induction Catalysis. *ACS Appl. Nano Mater.* **2021**, *4* (12), 13778−13787.
(32) Wang, W.; Duong-Viet, C.; Xu, Z.; Ba, H.; Tuci, G.; Giambastiani, G.; Liu, Y.; Truong-Huu, T.; Nhut, J. M.; Pham-Huu, C. CO_2 Methanation under Dynamic Operational Mode Using Nickel Nanoparticles Decorated Carbon Felt (Ni/OCF) Combined with Inductive Heating. *Catal. Today* **2020**, *357*, 214−220.
(33) Yang, X.; Wang, A.; Qiao, B.; Li, J. U. N.; Liu, J.; Zhang, T. Single-Atom Catalysts: A New Frontier in Heterogeneous Catalysis. *Acc. Chem. Res.* **2013**, *46* (8), 1740−1748.
(34) Ma, L.; Chen, X.; Li, J.; Chang, H.; Schwank, J. W. Electronic metal-support interactions in Pt/FeO nanospheres for CO oxidation. *Catal. Today* **2020**, *355*, 539−546.
(35) Lucci, F. R.; Liu, J.; Marcinkowski, M. D.; Yang, M.; Allard, L. F.; Flytzani-Stephanopoulos, M.; Sykes, E. C. H. Selective hydrogenation of 1,3-butadiene on platinum−copper alloys at the single-atom limit. *Nat. Commun.* **2015**, *6* (1), 8550.
(36) Neumann, S.; Doebler, H. H.; Keil, S.; Erdt, A. J.; Gutsche, C.; Borchert, H.; Kolny-Olesiak, J.; Parisi, J.; Bäumer, M.; Kunz, S. Effects of Particle Size on Strong Metal−Support Interactions Using Colloidal "Surfactant-Free" Pt Nanoparticles Supported on Fe 3 O 4. *ACS Catal.* **2020**, *10* (7), 4136−4150.
(37) Yang, M.; Allard, L. F.; Flytzani-Stephanopoulos, M. Atomically Dispersed Au−$(OH)_x$ Species Bound on Titania Catalyze the Low-Temperature Water-Gas Shift Reaction. *J. Am. Chem. Soc.* **2013**, *135* (10), 3768−3771.
(38) Yang, M.; Liu, J.; Lee, S.; Zugic, B.; Huang, J.; Allard, L. F.; Flytzani-Stephanopoulos, M. A Common Single-Site Pt(II)-$O(OH)_x$-Species Stabilized by Sodium on "Active" and "Inert" Supports Catalyzes the Water-Gas Shift Reaction. *J. Am. Chem. Soc.* **2015**, *137* (10), 3470−3473.
(39) Li, Z.; Geng, Y.; Ma, L.; Chen, X.; Li, J.; Chang, H.; Schwank, J. W. Catalytic Oxidation of CO over Pt/Fe_3O_4 Catalysts: Tuning O_2 Activation and CO Adsorption. *Front. Environ. Sci. Eng.* **2020**, *14* (4), 65.
(40) Wang, H.; Dong, J.; Allard, L. F.; Lee, S.; Oh, S.; Wang, J.; Li, W.; Shen, M.; Yang, M. Single-Site $Pt/La\text{-}Al_2O_3$ Stabilized by Barium as an Active and Stable Catalyst in Purifying CO and C_3H_6 Emissions. *Appl. Catal., B* **2019**, *244*, 327−339.
(41) Allian, A. D.; Takanabe, K.; Fujdala, K. L.; Hao, X.; Truex, T. J.; Cai, J.; Buda, C.; Neurock, M.; Iglesia, E. Chemisorption of CO and Mechanism of CO Oxidation on Supported Platinum Nanoclusters. *J. Am. Chem. Soc.* **2011**, *133* (12), 4498−4517.
(42) Steiner, U. E.; Ulrich, T. Magnetic Field Effects in Chemical Kinetics and Related Phenomena. *Chem. Rev.* **1989**, *89* (1), 51−147.
(43) Ren, X.; Wu, T.; Sun, Y.; Li, Y.; Xian, G.; Liu, X.; Shen, C.; Gracia, J.; Gao, H. J.; Yang, H.; Xu, Z. J. Spin-Polarized Oxygen Evolution Reaction under Magnetic Field. *Nat. Commun.* **2021**, *12* (1), 2608.
(44) Upadhyay, S.; Parekh, K.; Pandey, B. Influence of Crystallite Size on the Magnetic Properties of Fe_3O_4 Nanoparticles. *J. Alloys Compd.* **2016**, *678*, 478−485.
(45) Yan, J.; Wang, Y.; Zhang, Y.; Xia, S.; Yu, J.; Ding, B. Direct Magnetic Reinforcement of Electrocatalytic ORR/OER with Electromagnetic Induction of Magnetic Catalysts. *Adv. Mater.* **2021**, *33* (5), 2007525.
(46) Chen, R. R.; Chen, G.; Ren, X.; Ge, J.; Ong, S. J. H.; Xi, S.; Wang, X.; Xu, Z. J. SmCo5 with a Reconstructed Oxyhydroxide Surface for Spin-Selective Water Oxidation at Elevated Temperature. *Angew. Chem. Int. Ed.* **2021**, *60* (49), 25884−25890.
(47) Sun, T.; Tang, Z.; Zang, W.; Li, Z.; Li, J.; Li, Z.; Cao, L.; Sebastian, J.; Rodriguez, D.; Mariano, C. O. M.; Xu, H.; Lyu, P.; Hai, X.; Lin, H.; Sheng, X.; Shi, J.; Zheng, Y.; Lu, Y.; He, Q.; Chen, J. Ferromagnetic Single-Atom Spin Catalyst for Boosting Water Splitting. *Nat. Nanotechnol.* **2023**, *18* (7), 763−771.
(48) Ge, J.; Ren, X.; Chen, R. R.; Sun, Y.; Wu, T.; Ong, S. J. H.; Xu, Z. J. Multi-Domain versus Single-Domain: A Magnetic Field Is Not a Must for Promoting Spin-Polarized Water Oxidation. *Angew. Chem. Int. Ed.* **2023**, *62* (26), No. e202301721.
(49) Melander, M.; Laasonen, K.; Jónsson, H. Effect of Magnetic States on the Reactivity of an FCC(111) Iron Surface. *J. Phys. Chem. C* **2014**, *118* (29), 15863−15873.
(50) Sá, J.; Szlachetko, J.; Sikora, M.; Kavčič, M.; Safonova, O. V.; Nachtegaal, M. Magnetic Manipulation of Molecules on a Non-Magnetic Catalytic Surface. *Nanoscale* **2013**, *5* (18), 8462−8465.
(51) Gathmann, S. R.; Ardagh, M. A.; Dauenhauer, P. J. Catalytic Resonance Theory: Negative Dynamic Surfaces for Programmable Catalysts. *Chem. Catal.* **2022**, *2* (1), 140−163.

https://doi.org/10.1021/acscatal.3c05989
ACS Catal. 2024, 14, 4008−4017